Frequency-comb-calibrated swept-wavelength interferometry

Research Article | Vol. 29, No. 15 / 19 July 2021 / Optics Express 24363
Optics EXPRESS

Frequency-comb-calibrated swept-wavelength interferometry

KRISHNA TWAYANA,* ZHICHAO YE, ÓSKAR B. HELGASON, KOVENDHAN VIJAYAN, MAGNUS KARLSSON, AND VICTOR TORRES-COMPANY

Department of Microtechnology and Nanoscience (MC2), Photonics Laboratory Chalmers University of Technology, SE-41296, Sweden
*twayana@chalmers.se

Abstract: Lasers are often used to characterize samples in a non-destructive manner and retrieve sensing information transduced in changes in amplitude and phase. In swept wavelength interferometry, a wavelength-tunable laser is used to measure the complex response (i.e. in amplitude and phase) of an optical sample. This technique leverages continuous advances in rapidly tunable lasers and is widely used for sensing, bioimaging and testing of photonic integrated components. However, the tunable laser requires an additional calibration step because, in practice, it does not tune at a constant rate. In this work, we use a self-referenced frequency comb as an optical ruler to calibrate the laser used in swept-wavelength interferometry and optical frequency domain reflectometry. This allows for realizing high-resolution complex spectroscopy over a bandwidth exceeding 10 THz. We apply the technique to the characterization of low-loss integrated photonic devices and demonstrate that the phase information can disentangle intrinsic from coupling losses in the characterization of high-Q microresonators. We also demonstrate the technique in reflection mode, where it can resolve attenuation and dispersion characteristics in integrated long spiral waveguides.

1. Introduction

Swept wavelength interferometry (SWI) is a highly sensitive and versatile technique used in industrial and scientific applications, like biomedical imaging [1,2], distributed sensing [3], characterization of fibers [4,5] and integrated photonic device measurements [6,7]. SWI is a particular modality of linear spectral interferometry [8] whereby the sample under test is placed in one of the arms of an unbalanced interferometer. A key advantage of SWI is that it benefits from the rapid development of fast continuously tunable lasers. In SWI, the spectral information is captured in the time domain with the aid of a real-time-sampling oscilloscope or an analog to digital converter unit. With lasers exceeding sweep speeds of 10,000 nm/s [9], an ultrabroad bandwidth can be rapidly captured with a frequency resolution that is fundamentally limited by the laser instantaneous linewidth. Unfortunately, the wavelength of the laser never really tunes linearly in time. As a result, additional setups are needed that aid the calibration of the time axis into optical frequency [7,10,11]. These setups are usually based on auxiliary interferometers that are subject to environmental perturbations, and their inherent dispersion introduces systematic errors in the frequency calibration of the tunable laser used for SWI.

Laser frequency combs can be used as precise and accurate optical frequency rulers against which to calibrate tunable lasers [12,13]. Frequency comb-assisted tunable laser calibration has been successfully applied in the context of spectroscopy [12,14], absolute distance measurement [15,16] and imaging [17]. Furthermore, frequency combs allow for calibrating different laser bands while retaining absolute accuracy [14]. Here, we apply this calibration approach to SWI and illustrate its relevance for the characterization of low-loss integrated photonic components in

#430818 https://doi.org/10.1364/OE.430818
Journal © 2021 Received 5 May 2021; revised 8 Jul 2021; accepted 9 Jul 2021; published 16 Jul 2021

Optics EXPRESS

the telecommunications band. The precise laser calibration enables attaining simultaneously ultra-wide bandwidth, large dynamic range and ultra-high resolution – key performance metrics of an SWI system. We consider two different modalities, reflection and transmission. The reflection setup allows us to retrieve non-destructively both the propagation losses of long low-loss waveguides and their group velocity dispersion coefficient. The transmission approach allows access to the spectrally resolved phase information in comb-assisted laser spectroscopy [12,14]. We exemplify the technique with the characterization of high-Q dispersion-engineered microresonators and demonstrate that our comb-calibrated SWI allows us to distinguish coupling loss from intrinsic loss contributions in high-Q microresonators.

2. Principle and experimental setup

The experimental setup for the frequency-comb-assisted swept-wavelength interferometry is depicted in Fig. 1(a). An external cavity diode laser (ECDL) tunable within the telecommunications C & L bands (1520-1630 nm) is used as the tunable source. It has a narrow linewidth (10 kHz) and is mode-hop free, featuring a nearly constant tuning rate up to 10 nm/s. In order to calibrate the optical frequency axis, we follow a procedure similar to [12,18]. A fraction of the laser power is tapped off and heterodyned against a commercially available self-referenced fiber-based frequency comb source with 250 MHz line spacing. The signal detected by a balanced photodetector (BPD) is filtered with a radio-frequency bandpass filter (BPF) with center frequency $f_{BP} = 75$ MHz. This generates two distinct calibration markers every time the tunable laser frequency approaches a comb mode [12]. In order to resolve the mode number, a stable reference laser locked to an acetylene absorption line is used. This laser emits at a frequency known with a relative accuracy better than half the repetition rate of the comb. The reference markers generated by the beating of the tunable laser and the reference laser are detected by a photodetector (PD) followed by a BPF (central frequency 60 MHz). The peaks of the reference and calibration markers are tracked separately by two envelope detectors. The envelope detectors are biased with opposite polarity which drive the reference and calibration markers opposite to the zero-voltage level. This enables acquisition of the markers using a single channel and eases the identification of the reference and calibration markers in the off-line processing. The memory depth for each data acquisition channel is 100 million samples. This approach for calibrating the laser on the fly provides absolute accuracy over a broad tuning range. However, it is necessary to calibrate the nonlinearity of the laser also between consecutive modes. This is done with the aid of an additional Mach Zehnder fiber interferometer (MZI). The relative delay (τ) is assumed constant between consecutive markers, but the value varies across the laser tuning range of 10 THz due to the dispersion of the fiber. This is calibrated by measuring the change in phase between the two markers ($\triangle\ \emptyset$) and corresponding frequency difference ($\triangle f$) using $\tau = \triangle\ \emptyset/(2\pi\ \triangle f)$. The frequency difference ($\triangle f$) is given by the separation between consecutive beat markers and the MZI interference pattern is used to measure the phase difference ($\triangle\ \emptyset$).

We implemented two different arrangements for the characterization of a device under test (DUT). In the first configuration, the DUT is placed in a fiber-based Mach-Zehnder interferometer [Fig. 1(b)], wherein a fraction of the laser power probes the DUT and interferes with the reference signal at a coupler. The interference fringe pattern is mapped from the time domain to the frequency domain after the calibration of the laser. Then the optical frequency axis is discretized into equal intervals and its Fourier analysis allows retrieving the complex spectral response of the DUT. In the second configuration, the DUT is placed in a fiber-based reflectetric arrangement as shown in Fig. 1(c), adopting similar offline processing. However, there is a disparity between the two configurations in how the interference signals carry the optical properties. In the latter case, known as optical frequency domain reflectometry (OFDR) [7,10,19], the distributed backscattered light from the DUT is interfered with the reference signal, whereas interference occurs between light going through the DUT and reference arm in the former case (SWI).

Optics EXPRESS

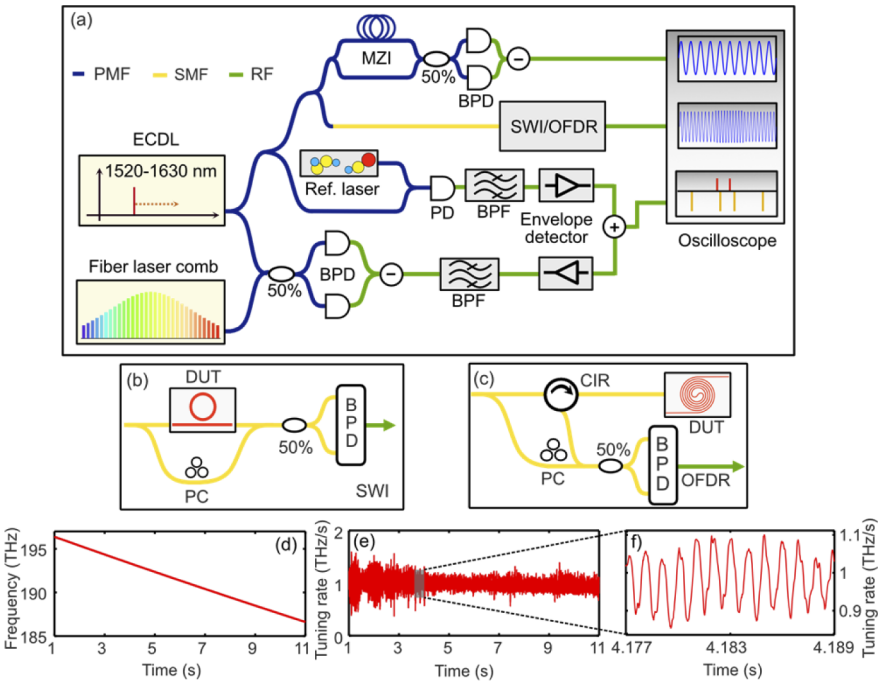

Fig. 1. Frequency comb calibrated swept-wavelength interferometry. (a) Measurement setup for the acquisition of frequency calibrated SWI/OFDR interference fringe pattern. Frequency calibration is achieved through beat markers provided by fiber frequency comb, a reference gas cell and the fiber MZI interference pattern. The acquisition of patterns in the boxes of an oscilloscope are from different channels. (b) Schematic of the swept-wavelength interferometry transmission configuration for the characterization of the microresonator. (c) Schematic of the optical-frequency-domain-reflectometry configuration for the characterization of the waveguide. (d) Calibrated laser frequency vs. time. (e) Measured tuning rate of the laser when set at 1 THz/s. (f) Zoom-in of the tuning rate.

Figure 1(d) shows the time to frequency mapping after the calibration performed with the laser frequency comb. The tuning rate is set to 1 THz/s considering the response time of RF filters and envelope detectors [12]. The maximum scanning speed is constrained by the slowest response time of the RF components. For a bandpass filter of 1 MHz bandwidth used in this work, it yields a maximum scanning speed of 1 THz per second. This nominal tuning rate roughly corresponds to 120 kHz sampling frequency resolution for a scanning period of twelve seconds. The optical frequency of the laser tunes in a quasi-linear fashion. The small deviations can be better accounted for when calculating the tuning rate, displayed in Fig. 1(e) and the zoomed in version in Fig. 1(f). While the tuning of the optical frequency is continuous over the measurement time, the rate varies significantly across the set value of 1 THz/s, resulting in an unevenly spaced SWI signal as a function of the calibrated frequency. The oscillatory nature of the tuning rate has been observed before with other fast tunable lasers used in the context of SWI [20].

3. Comb-calibrated SWI for characterization of high-Q microresonators

We illustrate the potential of the comb-calibrated SWI for the analysis of complex transmission spectra of high-Q microresonators. Comb-assisted broadband laser spectroscopy is often used to establish with high precision and accuracy the frequency location of the longitudinal modes in optical cavities [12,21–23]. In turn, this enables the retrieval of the group-velocity-dispersion

Optics EXPRESS

coefficient of different transverse mode families [12]. Measuring the transmission spectra of microresonators with fine spectral resolution over a broad bandwidth also allows for a quantitative estimate of the wavelength dependence of the loaded quality factor [24]. The loaded quality factor is composed of two loss contributions, intrinsic and coupling [25]. In conventional measurements of the transmission intensity spectrum, these loss contributions can only be unequivocally discriminated from each other when they contribute equally (i.e. under critical coupling condition). However, the introduction of the SWI allows to resolve the phase profile within the resonance, and thus the unambiguous retrieval of intrinsic and coupling loss rate without prior assumptions of the wavelength dependence of the coupling parameter.

Figure 2(a) is a schematic diagram of the SWI of a silicon nitride, high-Q microresonator, and a microscopic image (including a heater on the top) at the right. The microresonator is fabricated based on the approach described in [21], and has transversal dimensions $600 \times 1850\ \mathrm{nm}^2$, diameter 217 μm and 350 nm gap between the bus waveguide and ring. It has a tapered structure at both ends of the waveguide to prevent coupling to higher-order modes. The polarization controllers PC1 and PC2 were adjusted separately in sequence to optimize the coupling to the microresonator polarization state (quasi-TE) and co-polarize the signal from the reference and DUT arms. The polarization state at the input chip facet is stable. The amplitude response of the DUT modulates the envelope of the fringe pattern and the phase response is encoded in its oscillations. The relative optical path length delay between the arms was chosen so that several spectral fringes appear over a resonance linewidth. This ensures encoding of the phase of the resonances having different linewidths. In our measurement, the optical path difference was ~23 m (~115 ns) excluding the DUT, which corresponds to a fringe pattern period of $\Delta\vartheta = 1/\tau$ ~8 MHz. Because the loaded Q of the resonator corresponds to an average linewidth of ~56 MHz, there are seven MZI spectral periods on average per resonance.

In addition to the phase response of the DUT, the imbalance dispersion of the other optical components affects the interference pattern. The transfer phase function measurement of the DUT could be done in two sequential steps. First measuring the phase profile of the configuration without the DUT and then with the DUT inserted. The phase difference between these two measurements would correspond to the DUT phase function. However, in the particular case where the DUT is a microresonator, the calibration can be done with a single measurement including the DUT. The optical power coming out of the DUT arm is a superposition of light that traverses through the bus waveguide and a fraction of light coupled back into the waveguide from the ring in every round trip. There is interference between the signal from the DUT arm and the reference arm. We extracted the reference transfer function attributed to the shortest optical path (i.e. bus waveguide virtually without ring) $\mathcal{H}_{ref}$ and overall configuration $\mathcal{H}_{tot}$. The reference function also includes the response of parasitic interference fringes from the chip facets. The Fabry-Perot (FP) interference from 0.5 cm apart chip facets has a frequency period ~15 GHz. This is three orders of magnitude larger than the linewidth of the resonances. As such, the intrinsic FP interference response appears to be constant for the resonances. The complex response solely associated to the ring resonator alone is $\mathcal{H}_{ring} = \mathcal{H}_{tot}/\mathcal{H}_{ref}$. The argument of $\mathcal{H}_{ring}$ entails the linear phase factor, thus subtracting a linear fit results in the phase characteristic of the microresonator. Figure 2(b) is the normalized transmission scan and Fig. 2(c) is the phase response for the fundamental quasi-TE mode of a microresonor. The retrieved phase and the measured magnitude spectra for different coupling cases are presented in Fig. 2(d)-(f). All these figures are plotted for ~ 800 MHz abscissa range. The magnitude response in Fig. 2(d) and Fig. 2(e) are quite similar, however, the phase profile is distinct and corresponds to the over-coupling and under-coupling regime respectively. In Fig. 2(f), the transmission at the resonance location is zero and an abrupt effective phasensition of π radians (corresponding to critical coupling) is clearly observed.

Optics EXPRESS

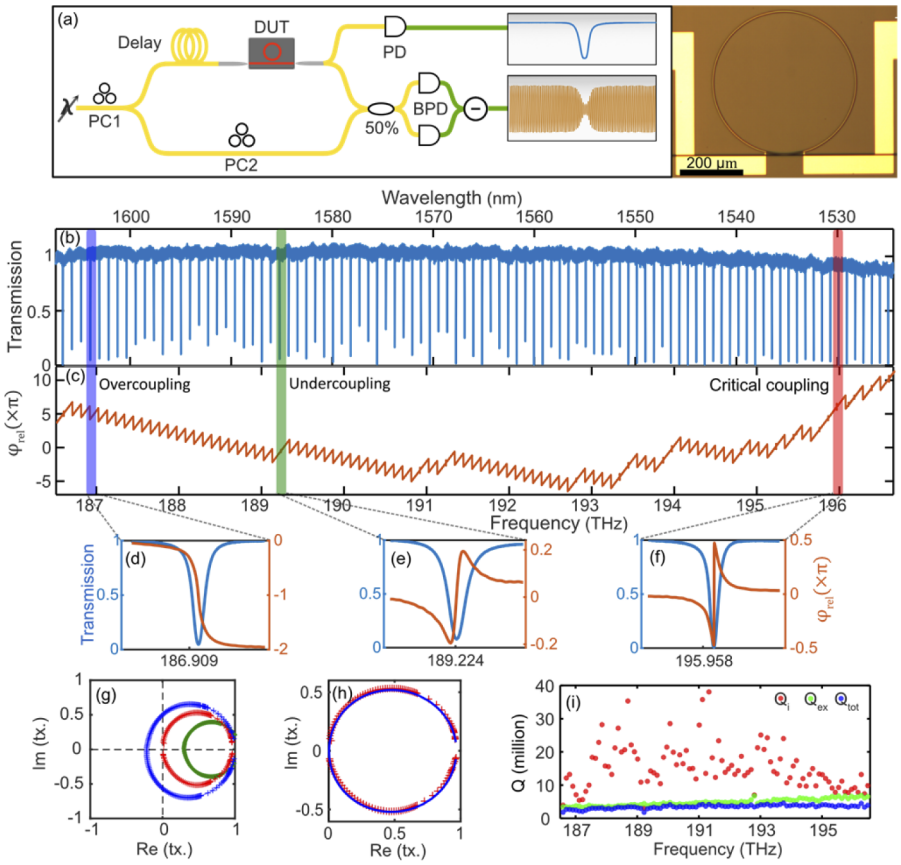

Fig. 2. SWI for spectral characterization of microresonator. (a) Measurement setup for acquisition of transmission trace and interferogram (microscopic image of microresonator is shown at righthand side). (b) Normalized transmission scan of microresonator. (c) Linearized effective phase response of the resonator. Different coupling conditions: (d) Over-coupling. (e) Under-coupling. (f) Critical coupling. (g) Phasor diagram of different coupling conditions. (h) Phasor diagram fit of the resonance in Fig. 2(f). (i) Intrinsic, extrinsic and total quality factor (Q_i, Q_{ex}, Q_{tot}) plot.

Optics EXPRESS

Given the implications of the limited delay length and corresponding frequency sampling, it was challenging to resolve the narrow resonance feature of high Q microresonator from the interferogram information. Therefore, the transmission scan directly recorded from the microresonator output was considered as magnitude response for the parametric fitting. Knowing the amplitude transmission (T) and the relative phase response (φ_{rel}), the complex transfer function of the resonance can be described as $|T|\exp(j\varphi_{rel})$ and represented in the complex (IQ) plane. The complex diagram representation of different resonance coupling conditions is illustrated in Fig. 2(g), in which the color of the plots corresponds to the response of microresonator highlighted by the same color bars in Fig. 2(b)-(c). The loop is traced counterclockwise as the effective phase proceeds from the positive to the negative side. The point crossing the real axis in the complex plane corresponds to the value at the resonance frequency (ω_0) and its sign is determined by the cosine of the relative phase φ_{rel} at ω_0 ($|\varphi_{rel}| = 0$ for undercouplinand π or 0 for overcoupling). Therefore, the origin is always outside of the loop for undercoupling.

The characteristic parameters of the resonances can be retrieved unambiguously from the Lorentzian model of transmission spectrum fitted with the aid of the distinct phase profiles [23,26]. However, small imperfections in the micro-ring lead to distributed backscattering, and coherent build-up of this reflected light can excite the counterclockwise (CCW) mode. The coupling between degenerate clockwise (CW) and CCW modes distorts the ideal Lorentzian spectrum and eventually leads to resonance-splitting [25,27]. In order to correctly model the resonances, a steady state solution of coupled mode theory (CMT) in the time domain has been widely adopted in the literature [28,29]. The free parameters of the steady-state solution in the frequency domain are fitted to the resonance transmission spectrum using a least-square algorithm. However, without prior knowledge of the coupling condition there exists an ambiguity in the retrieved coefficients. In addition, we noticed that the fitting may result in different solutions depending on the initial guess for the fitting. In contrast, parametric fitting of the complex resonance spectrum returns an unambiguous and consistent set of coefficients as the fitting equation has a unique functional dependence on the coupling rates, i.e. intrinsic coupling κ_0, extrinsic coupling κ_{ex}, and mutual coupling κ_c.

The majority of the resonances across the measurement range display a continuous sigmoid-like phase transition of 2π, thus indicating an overcoupling condition ($\kappa_0 < \kappa_{ex}$). However, some resonances have a reverse phase transition near the resonance because of a stronger coupling to a counterpropagating mode [30,31]. These resonances are still overcoupled because the phase variation is significantly higher than that for the undercoupled case. In Fig. 2(f), there is a zero transmission and an abrupt π phase shift at the resonance location. We identify it as a critically coupled resonance. For this distinct resonance, the mutual coupling coefficient $\kappa_c = \sqrt{|\kappa_{ex}^2 - \kappa_0^2|}$ [30]. The blue quasi-circle in Fig. 2(h) is the parametric complex split resonance fit of this resonance. It has $\kappa_0/2\pi = 22.6$ MHz, $\kappa_{ex}/2\pi = 29.8$ MHz, $\kappa_c/2\pi = (19.6 + 0.4\,i)$ MHz i.e. $|\kappa_c{}^2| \sim |\kappa_{ex}^2 - \kappa_0^2|$, whereas the parametric fitting without considering the phase response does not satisfy this condition. The other resonances with reverse phase transition have a wider resonance linewidth. This is due to the further increase of κ_c, but not enough to cause resonance splitting, which occurs when $\kappa_c{}^2 > |\kappa_{ex}^2 - \kappa_0^2|$. After the evaluation of coupling coefficients, it is trivial to calculate the quality factors; intrinsic Q-factor $Q_i = \omega_0/\kappa_0$, extrinsic Q-factor $Q_{ex} = \omega_0/\kappa_{ex}$ and the total Q-factor $1/Q_{tot} = 1/Q_i + 1/Q_{ex}$. Figure 2(i) is the quality factor plot of the high-Q microresonator, having an average intrinsic Q of 15 million. The resonance linewidth is sufficiently large to neglect ringing artifacts. The variation of intrinsic Q for different resonances is attributed to the wavelength dependent transversal mode coupling and N-H bond absorption. The resonance at the frequency 189.224 THz has $Q_i < Q_{ex}$ ($\kappa_0/2\pi = 62$ MHz, $\kappa_{ex}/2\pi = 42$ MHz) which is an example of the undercoupling condition. Near this resonance, there was a tiny shallow notch and the analysis of the integrated dispersion (D_{int}, not shown) indicated a clear mode crossing. We believe that the existence of an undercoupled resonance in the middle

Optics EXPRESS

of overcoupled resonances is because of the strong power coupling to a higher-order mode, resulting in a broader resonance linewidth. From the integrated dispersion coefficients, the converted dispersion value is 70 ± 1 ps^2/km at 1550 nm which is close to our simulation result of 74 ps^2/km.

4. Comb calibrated OFDR for characterization of low loss spiral waveguides

Optical frequency domain reflectometry (OFDR) is a prevalent technique for characterizing integrated optical devices and fiber assemblies [7,10,19,32,33]. It is a high-sensitive and non-destructive optical measurement technique. However, there are some challenges when it comes to implementing this technique for integrated devices. The dispersion of an integrated device limits the spatial resolion. This prevents dealing with integrated devices having small feature sizes. On the other hand, the reflective nature intrinsic to the cleaved facets of the integrated waveguides can be exploited in the OFDR to estimate the group refractive index [33]. As in SWI, it is of utmost importance to precisely calibrate the tuning of the laser. The laser can be calibrated with an auxiliary interferometer by applying the dispersion correction function [19], but it requires a precise calibration of the fiber delay and should be operated in a stable condition. In the following, we will present the comb-calibrated OFDR for characterization of a Si_3N_4 spiral waveguide. The comb calibration enables higher precision in the phase measurement over an ultra-wide bandwidth range with fine spectral resolution. The waveguide propagation loss is measured assuming the reflectivity profile is uniform throughout the waveguide.

Figure 3(a) shows the schematic diagram of the OFDR in a Mach-Zehnder configuration for the characterization of a long waveguide (2036×700 nm^2) composed of multiple concatenated spirals. The microscopic image of a unit spiral waveguide is shown to the right of Fig. 3(a). The mode profile of the fundamental TE mode is illustrated in Fig. 3(b). The length of a waveguide is ~1.5 m comprising 25 cascaded spiral units. The spectral and spatial properties of the DUT is embedded on the light reflected from the rear facet. The interference of the reflected signal with the reference signal generates an interference pattern. After offline processing, the time axis of the interference pattern was converted into a frequency axis and discretized into equally spaced frequency points. Then, its inverse Fourier transform resulted in a spatial reflectivity profile [Fig. 3(c) for TE mode and Fig. 3(d) for TM mode]. The two dominant peaks were attributed to the reflection from the front and rear facets. These peaks were clipped by a windowing function. Subsequently, the Fourier transform operation is performed to get the response back into the spectral domain. This allowed for extracting the transfer function of the system virtually without the DUT ($\mathcal{H}_{ref}$) and the overall response including a round trip of the DUT ($\mathcal{H}_{tot}$). Finally, the effective phase response of the DUT ($\emptyset_{eff}$) was calculated by $\arg(\mathcal{H}_{tot}) - \arg(\mathcal{H}_{ref})$, followed by subtracting a linear fit.

The unbalanced dispersion of the fiber interferometer affects the impulse response of the individual reflection peaks, but not the relative phase difference. In Fig. 3(c), the second reflection peak (blue in the inset) is broader than the first reflection peak (red), which indicates that both the unbalanced fiber dispersion and DUT dispersion are in the same dispersion regime (anomalous). However, the second reflection peak is narrower in Fig. 3(d) because the net differential dispersion of the interferometer partially compensates for the dispersion of the DUT. The reflectivity profile in between the two reflection peaks accounts for the distributed loss of the waveguide. The average propagation loss in the waveguide (excluding the facets losses) was estimated by the gradient of the reflectivity. The propagation loss measured from the distributed backscattering was 4.26 ± 0.04 dB/m for the TE mode and 4.66 ± 0.04 dB/m for the TM mode. The uncertainty is estimated as a 95% confidence interval of the fitting. The quasi-linear relationship in the backscattered power reflects negligible bending loss and fabrication defects. Finally, a dynamic range greater than 80 dB was measured over a bandwidth >10 THz. This is higher than the dynamic range measured for other spiral waveguides with the conventional OFDRs [34,35].

Optics EXPRESS

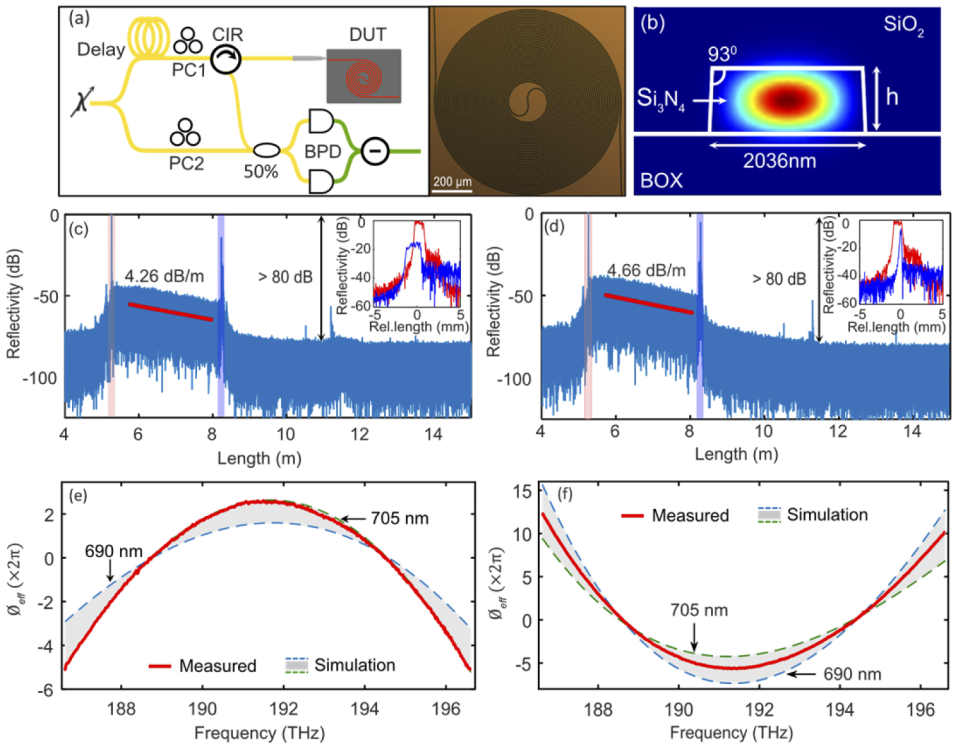

Fig. 3. OFDR for characterization of the waveguide. (a) Schematic of OFDR measurement setup and microscopic image of the spiral waveguide. (b) Fundamental TE mode profile. (c) Spatial reflectivity of fundamental quasi-TE mode (Inset: zoom in of reflection peaks). (d) Spatial reflectivity of fundamental quasi-TM mode (Inset: zoom in of reflection peaks). (e) TE mode measured and simulated effective phase response plot normalized by 2π. (f) TM mode measured and simulated effective phase response plot normalized by 2π.

The measured phase responses, red curve in Fig. 3(e) for fundamental quasi-TE mode and red curve in Fig. 3(f) for quasi-TM mode, have a spectral resolution of 1 MHz over >10 THz bandwidth. To verify the dispersion value provided by the OFDR measurement, numerical simulations using a finite element solver (COMSOL) were performed for various waveguide dimensions considering both the waveguide geometry and the bulk material indices measured by ellipsometry. The phase response was calculated by the Taylor expansion of the propagation constant of the mode and considering the round-trip length of the waveguide. The grey color pattern illustrates the simulated effective phase profile normalized by 2π for the waveguide dimensions of width 2036 nm and height 690-705 nm for TE and TM modes. There is a good agreement between the measured and simulated effective phase considering a fabrication uncertainty of ~10 nm in the waveguide height arising from an inhomogeneous film in the deposition. For the TE mode, the measured phase profile followed a convex parabolic symmetry, and a concave parabolic profile for the TM mode. The fit to a third-order dispersion profile resulted in anomalous and normal dispersion values, respectively. To test the accuracy, we performed the dispersion measurement without the comb calibration, using only the auxiliary MZI calibration. Table 1 illustrates the second (i.e. group velocity dispersion coefficient, GVD) and third-order-dispersion values estimated for the TE and TM modes at 1550 nm for a waveguide of dimensions 2036×700 nm^2 by the different techniques. The table clearly shows the importance of the comb calibration for the dispersion measurement of the waveguides.

Optics EXPRESS

Table 1. Comparison of dispersion values estimated by frequency Comb, MZI laser frequency calibration and FDE simulation for the TE and TM modes. Here, the waveguide dimension is 2036×700 nm^2 and dispersion value is calculated at 1550 nm.

Dispersion coefficient	TE mode			TM mode		
	Comb	MZI	Simulation	Comb	MZI	Simulation
β_2 (ps^2/km)	−33	−0.6	−31	59	92	50
β_3 (ps^3/km)	−0.05	−0.3	− 0.14	−1.2	−1.4	−1.4

5. Conclusion

Swept wavelength interferometry forms the basis for wideband spectral characterization of photonic devices. However, it lacks absolute accuracy and suffers from a systematic error that arises the laser nonlinear tuning. We have calibrated the tunable laser with the aid of a self-referenced frequency comb and studied its advantages in SWI and OFDR for broadband spectral characterizations of ultra-low loss Si_3N_4 components. In SWI, we could unravel the ambiguity that appears when distinguishing extrinsic from intrinsic coupling coefficients in the measurement of high-Q microresonators. In the OFDR configuration, the precise laser calibration enabled us measuring the effective phase response for a bandwidth > 10 THz with a resolution ∼1 MHz and dynamic range of > 80 dB. We exemplified the technique with long dispersion-engineered low-loss silicon nitride waveguides. The measured phase allowed to resolve the distributed loss of the waveguides and retrieve the dispersion coefficients, which showed a good agreement with the simulation results.

Funding. Horizon 2020 Framework Programme (GA 812818); European Research Council (GA 771410); Vetenskapsrådet (2015-00535, 2016-03960, 2016-06077, 2020-00453).

Acknowledgements. The Si_3N_4 devices were fabricated at Myfab Chalmers.

Disclosures. The authors declare no conflict of interest.

Data availability. The raw data of the measurement results within this work is accessible [36].

References

1. S. H. Yun, G. J. Tearney, J. F. De Boer, N. Iftimia, and B. E. Bouma, "High-speed optical frequency-domain imaging," Opt. Express **11**(22), 2953–2963 (2003).
2. T. Klein and R. Huber, "High-speed OCT light sources and systems," Biomed. Opt. Express **8**(2), 828–859 (2017).
3. M. Froggatt and J. Moore, "High-spatial-resolution distributed strain measurement in optical fiber with Rayleigh scatter," Appl. Opt. **37**(10), 1735–1740 (1998).
4. J. P. Von Der Weid, R. Passy, G. Mussi, and N. Gisin, "On the characterization of optical fiber network components with optical frequency domain reflectometry," J. Lightwave Technol. **15**(7), 1131–1141 (1997).
5. H. Chen, N. K. Fontaine, J. C. Alvarado-Zacarias, C. Cheng, M. Bigot, P. Sillard, R. Ryf, M. Mazur, D. T. Neilson, R. Amezcua-Correa, and M. Yang, "Multiport swept-wavelength interferometer with laser phase noise mitigation employing a broadband ultra-weak FBG array," Opt. Lett. **45**(21), 5913–5916 (2020).
6. J. F. Bauters, M. J. R. Heck, D. D. John, J. S. Barton, C. M. Bruinink, A. Leinse, R. G. Heideman, D. J. Blumenthal, and J. E. Bowers, "Planar waveguides with less than 01 dB/m propagation loss fabricated with wafer bonding," Opt. Express **19**(24), 24090–24101 (2011).
7. L. A. Bru, D. Pastor, and P. Muñoz, "Integrated optical frequency domain reflectometry device for characterization of complex integrated devices," Opt. Express **26**(23), 30000–30008 (2018).
8. A. M. Weiner, *Ultrafast Optics* (Wiley, 2009).
9. E. V Andreeva, L. N. Magdich, D. S. Mamedov, A. A. Ruenkov, M. V Shramenko, and S. D. Yakubovich, "Tunable semiconductor laser with an acousto-optic filter in an external fibre cavity," Quantum Electron. **36**(4), 324–328 (2006).
10. B. J. Soller, D. K. Gifford, M. S. Wolfe, and M. E. Froggatt, "High resolution optical frequency domain reflectometry for characterization of components and assemblies," Opt. Express **13**(2), 666 (2005).
11. M. Badar, P. Lu, M. Buric, and P. Ohodnicki, "Integrated auxiliary interferometer for self-correction of nonlinear tuning in optical frequency domain reflectometry," J. Lightwave Technol. **38**(21), 6097–6103 (2020).
12. P. Del'Haye, O. Arcizet, M. L. Gorodetsky, R. Holzwarth, and T. J. Kippenberg, "Frequency comb assisted diode laser spectroscopy for measurement of microcavity dispersion," Nat. Photonics **3**(9), 529–533 (2009).

Optics EXPRESS

13. I. Coddington, F. R. Giorgetta, E. Baumann, W. C. Swann, and N. R. Newbury, "Characterizing fast arbitrary CW waveforms with 1500 THz/s instantaneous chirps," IEEE J. Sel. Top. Quantum Electron. **18**(1), 228–238 (2012).
14. J. Liu, V. Brasch, M. H. P. Pfeiffer, A. Kordts, A. N. Kamel, H. Guo, M. Geiselmann, and T. J. Kippenberg, "Frequency-comb-assisted broadband precision spectroscopy with cascaded diode lasers," Opt. Lett. **41**(13), 3134–3137 (2016).
15. E. Baumann, F. R. Giorgetta, I. Coddington, L. C. Sinclair, K. Knabe, W. C. Swann, and N. R. Newbury, "Comb-calibrated frequency-modulated continuous-wave ladar for absolute distance measurements," Opt. Lett. **38**(12), 2026–2028 (2013).
16. W. Yu, P. Pfeiffer, A. Morsali, J. Yang, and J. Fontaine, "Comb-calibrated frequency sweeping interferometry for absolute distance and vibration measurement," Opt. Lett. **44**(20), 5069–5072 (2019).
17. E. Baumann, F. R. Giorgetta, J.-D. Deschênes, W. C. Swann, I. Coddington, and N. R. Newbury, "Comb-calibrated laser ranging for three-dimensional surface profiling with micrometer-level precision at a distance," Opt. Express **22**(21), 24914–24928 (2014).
18. M. H. P. Pfeiffer, C. Herkommer, J. Liu, T. Morais, M. Zervas, M. Geiselmann, and T. J. Kippenberg, "Photonic damascene process for low-loss, high-confinement silicon nitride waveguides," IEEE J. Sel. Top. Quantum Electron. **24**(4), 1–11 (2018).
19. I. Waveguides, U. Glombitza, and E. Brinkmeyer, "Coherent Frequency-Domain Reflectometry for Characterization of Single-Mode Integrated-Optical Waveguides," J. Lightwave Technol. **11**(8), 1377–1384 (1993).
20. E. D. Moore, "Advances in Swept-Wavelength Interferometry for Precision Measurements," Ph.D. dissertation, Electrical, Computer & Energy Engineering, University of Colorado, Boulder, CO (2011).
21. Z. Ye, K. Twayana, P. A. Andrekson, and V. Torres-Company, "High-Q Si_3N_4 microresonators based on a subtractive processing for Kerr nonlinear optics," Opt. Express **27**(24), 35719–35727 (2019).
22. S. Fujii and T. Tanabe, "Dispersion engineering and measurement of whispering gallery mode microresonator for Kerr frequency comb generation," Nanophotonics **9**(5), 1087–1104 (2020).
23. Y. Xuan, Y. Liu, L. T. Varghese, A. J. Metcalf, X. Xue, P.-H. Wang, K. Han, J. A. Jaramillo-Villegas, A. Al Noman, C. Wang, S. Kim, M. Teng, Y. J. Lee, B. Niu, L. Fan, J. Wang, D. E. Leaird, A. M. Weiner, and M. Qi, "High-Q silicon nitride microresonators exhibiting low-power frequency comb initiation," Optica **3**(11), 1171–1180 (2016).
24. L. Wu, H. Wang, Q. Yang, Q. Ji, B. Shen, C. Bao, M. Gao, and K. Vahala, "Greater than one billion Q factor for on-chip microresonators," Opt. Lett. **45**(18), 5129–5131 (2020).
25. W. Bogaerts, P. de Heyn, T. van Vaerenbergh, K. de Vos, S. Kumar Selvaraja, T. Claes, P. Dumon, P. Bienstman, D. van Thourhout, and R. Baets, "Silicon microring resonators," Laser Photonics Rev. **6**(1), 47–73 (2012).
26. J. E. Heebner, V. Wong, A. Schweinsberg, R. W. Boyd, and D. J. Jackson, "Optical transmission characteristics of fiber ring resonators," IEEE J. Quantum Electron. **40**(6), 726–730 (2004).
27. A. Li, T. Van Vaerenbergh, P. De Heyn, P. Bienstman, and W. Bogaerts, "Backscattering in silicon microring resonators: A quantitative analysis," Laser Photonics Rev. **10**(3), 420–431 (2016).
28. M. H. P. Pfeiffer, J. Liu, A. S. Raja, T. Morais, B. Ghadiani, and T. J. Kippenberg, "Ultra-smooth silicon nitride waveguides based on the Damascene reflow process: fabrication and loss origins," Optica **5**(7), 884–892 (2018).
29. K. Wu and A. W. Poon, "Stress-released Si 3 N 4 fabrication process for dispersion-engineered integrated silicon photonics," Opt. Express **28**(12), 17708–17722 (2020).
30. Q. Li, Z. Zhang, J. Wang, M. Qiu, and Y. Su, "Fast light in silicon ring resonator with resonance-splitting," Opt. Express **17**(2), 933–940 (2009).
31. Q. Li, T. Wang, Y. Su, M. Yan, and M. Qiu, "Coupled mode theory analysis of mode-splitting in coupled cavity system," Opt. Express **18**(8), 8367–8382 (2010).
32. F. Morichetti, A. Canciamilla, C. Ferrari, M. Torregiani, A. Melloni, and M. Martinelli, "Roughness induced backscattering in optical silicon waveguides," Phys. Rev. Lett. **104**(3), 1–4 (2010).
33. D. Zhao, D. Pustakhod, K. Williams, and X. Leijtens, "High Resolution Optical Frequency Domain Reflectometry for Analyzing Intra-Chip Reflections," IEEE Photonics Technol. Lett. **29**(16), 1379–1382 (2017).
34. M. A. Tran, D. Huang, T. Komljenovic, J. Peters, A. Malik, and J. E. Bowers, "Ultra-low-loss silicon waveguides for heterogeneously integrated silicon/III-V photonics," Appl. Sci. **8**(7), 1139 (2018).
35. Y. Li, K. Zhu, Z. Kang, W. L. Ho, R. Davidson, C. Lu, B. E. Little, and S. T. Chu, "CMOS-compatible high-index doped silica waveguide with an embedded silicon-nanocrystal strip for all-optical analog-to-digital conversion," Photonics Res. **7**(10), 1200–1208 (2019).
36. K. Twayana, "Raw data for: Frequency-Comb-Assisted Swept-Wavelength Interferometry," Zenodo: Version 1, 8 July 2021, https://zenodo.org/record/5083349.